ACS Photonics

pubs.acs.org/journal/apchd5

Letter

Phonon-Enhanced Mid-Infrared CO_2 Gas Sensing Using Boron Nitride Nanoresonators

Nestor Jr. Bareza, Bruno Paulillo,* Tetiana M. Slipchenko, Marta Autore, Irene Dolado, Song Liu, James H. Edgar, Saül Vélez, Luis Martín-Moreno, Rainer Hillenbrand, and Valerio Pruneri

Cite This: *ACS Photonics* 2022, 9, 34−42

Read Online

ACCESS | Metrics & More | Article Recommendations | Supporting Information

ABSTRACT: Hexagonal boron nitride (hBN) hosts long-lived phonon polaritons, yielding a strong mid-infrared (mid-IR) electric field enhancement and concentration on the nanometer scale. It is thus a promising material for highly sensitive mid-IR sensing and spectroscopy. In addition, hBN possesses high chemical and thermal stability as well as mechanical durability, making it suitable for operation in demanding environments. In this work, we demonstrate a mid-IR CO_2 gas sensor exploiting phonon polariton (PhP) modes in hBN nanoresonators functionalized by a thin CO_2-adsorbing polyethylenimine (PEI) layer. We find that the PhP resonance shifts to lower frequency, weakens, and broadens for increasing CO_2 concentrations, which are related to the change of the permittivity of PEI upon CO_2 adsorption. Moreover, the PhP resonance exhibits a high signal-to-noise ratio even for small ribbon arrays of 30 × 30 μm^2. Our results show the potential of hBN nanoresonators to become a novel platform for miniaturized phonon-enhanced SEIRA gas sensors.

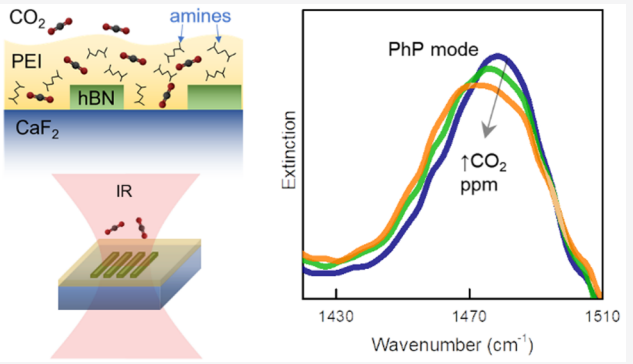

KEYWORDS: *boron nitride, phonon-polaritons, gas sensor, SEIRA*

Mid-infrared (mid-IR) spectroscopy is a powerful technique that directly probes vibrational fingerprints of molecules (e.g., gas, biomarkers, etc.), providing specificity and structural information on molecular bonds in non-destructive fashion. This is the basis of spectroscopic gas detection devices, among which the nondispersive infrared (NDIR) sensor is arguably the most popular.[1] It consists of a gas cell, IR source and detector, and allows quantification of gas concentration through characteristic IR absorption. However, such a simple setup suffers from cross-sensitivity to different gases, not allowing selectivity since their vibrations can overlap in frequency.[2] Also, the gas chamber of NDIR is typically bulky to counteract low cross-section IR interaction with gas molecules. Alternative techniques have been developed to enhance the light−gas interaction such as cavity-enhanced absorption spectroscopy (CEAS),[3] cavity ring-down spectroscopy (CRDS),[4] and quartz-enhanced photoacoustic spectroscopy (QEPAS).[5] For spectroscopic sensing, the optical setup can be miniaturized by implementing surface enhanced infrared absorption (SEIRA) schemes, where resonant nanostructures (e.g., antennas,[6] split ring resonators,[7] nanoholes[8]) create highly confined optical fields that greatly enhance light−matter interaction. SEIRA exceptionally improves the sensitivity of detection, allowing analysis of even minute amounts of analytes.

Most established materials for SEIRA sensors are noble metal (e.g., Au) thin films. However, they exhibit lossy plasmon modes (typical quality factor $Q \approx 10$)[9] with a relatively large evanescent field decay. Newly contending materials include nanostructured graphene that supports highly confined localized surface plasmon resonances (LSPRs) that can be tuned by either electrostatic[10] or chemical doping.[11] Graphene LSPR modes, however, have low extinction, typically a few %, and poor Q factors (typical $Q \approx 4$),[12], which limit the strength of light-molecular interaction and signal-to-noise ratio. Emerging alternatives are van der Waals crystals supporting volume- and surface-confined phonon polaritons (PhPs) modes with long lifetimes.[13−18] PhPs arise from the coupling between electromagnetic radiation and crystal lattice vibrations in the material. In particular, nanostructured hexagonal boron nitride (hBN) exhibits resonant PhP modes with high quality factors.[13,19] High-Q resonances ($Q \sim 10^2$) of natural[13] and monoisotopic hBN[15] nanoresonators were recently employed

Received: August 18, 2021
Published: January 5, 2022

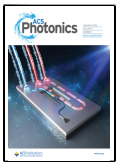

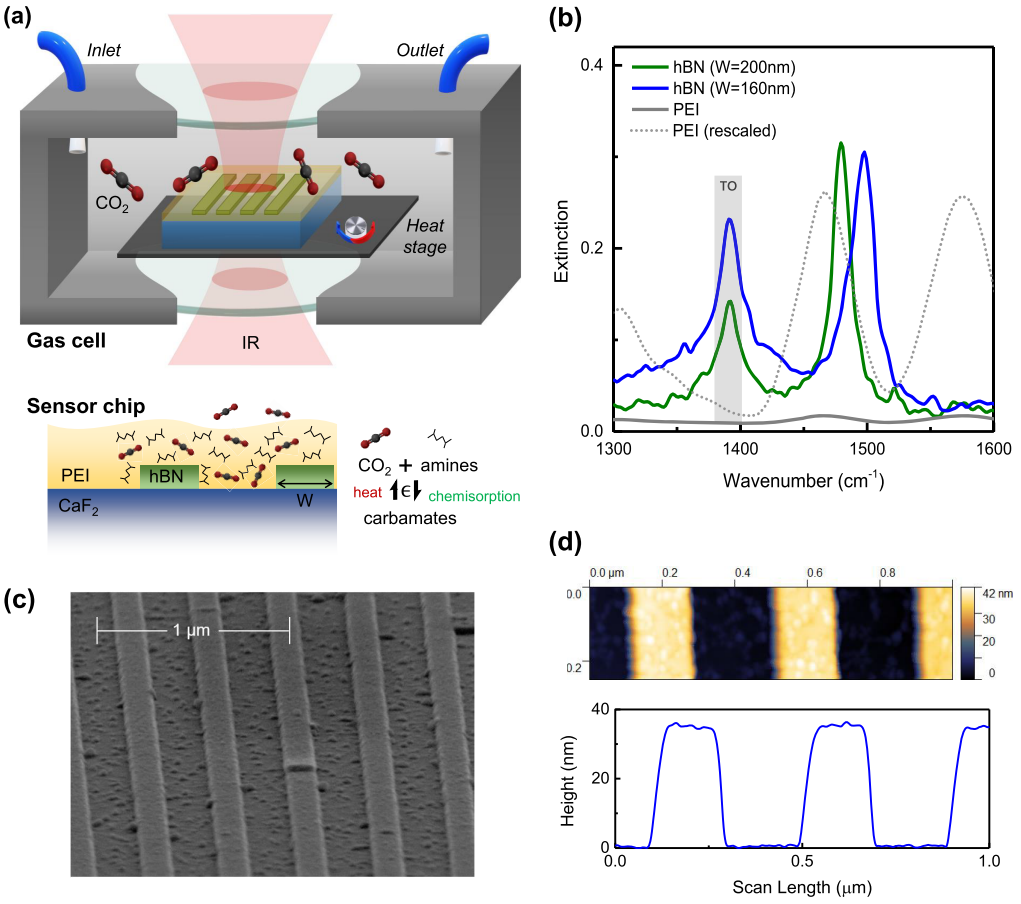

Figure 1. (a) Schematic diagram of the IR gas sensing setup consisting of a sensor chip placed on a heating stage embedded in a gas cell with IR-transmitting windows. The sensor chip consists of hBN nanoribbons fabricated on CaF_2 substrate with a 75 nm PEI layer coating. The cross-section sketch shows reversible chemisorption and thermal desorption of CO_2 molecules in the amine-rich PEI layer. (b) Experimental extinction spectra of hBN nanoribbons (without PEI layer) of two different widths and 400 nm period. For comparison, the extinction spectrum for 75 nm PEI on CaF_2 is shown (solid gray) and rescaled (dashed gray) to highlight vibrational overlap with PhP modes. (c) Scanning electron microscope (SEM) and (d) atomic force microscopy (AFM) characterizations of fabricated hBN nanoribbons.

to demonstrate molecular sensing at the strong coupling limit.[19,20]

The main challenge for using hBN and other 2D materials as gas sensors is the inherently poor physisorption of gas molecules on 2D nanostructures; the near-field interaction of the gases with the surface modes is weak. Functionalizing the nanostructures using a gas-adsorbing thin layer can solve this issue by concentrating the gas molecules inside the polariton field. For instance, thin films of polyethylenimine (PEI) polymer were shown to selectively adsorb CO_2 and could be regenerated through thermal desorption.[21] Efficient optical CO_2 detection was demonstrated with PEI deposited on resonant nanostructures surfaces such as metal metasurfaces,[22,23] graphene nanostructures,[24] and all-dielectric photonic crystal slab.[25]

In this work, we demonstrate phonon-enhanced mid-IR gas sensing using monoisotopic hBN nanoribbon arrays functionalized with a thin CO_2-adsorbing PEI layer. By recording the far-field transmission spectra of the PEI-coated ribbon arrays, we show PhP resonance modulation dependent on CO_2 concentration. We also demonstrate reversible optical response by thermally desorbing CO_2 molecules from PEI. The main added value of hBN with respect to contending materials (e.g., metals,[22] graphene[24]) is the high Q (~100) of the PhP resonances within the Reststrahlen region. This is advantageous for gas selectivity because one specific gas-sensitive PEI vibrational mode can be targeted, unlike metal or graphene plasmonic nanostructures ($Q \lesssim 10$), where multiple vibrations overlap with the resonant mode. The proposed hybrid material sensing platform, leveraging the high Q, and high extinction PhP modes can potentially become a miniaturized sensor component for indoor air quality (IAQ) monitoring and smart ventilation systems.[26,27]

The gas sensing setup and proposed hybrid-material sensor chip are sketched in Figure 1a. The gas cell with IR-transmitting windows is mounted in a Fourier Transform IR (FTIR) microscope operated in transmission mode. Inside the gas cell, the sensor chip is placed on a heating stage, and CO_2 gas is introduced through gas valves. The sensor chip consists of monoisotopic hBN nanoribbons on a CaF_2 substrate, which exhibit transversal volume-confined PhP Fabry–Perot resonances.[19,20] They are covered with a PEI thin layer. The sketch conceptualizes the chemisorption of CO_2 molecules in the PEI layer which interact with amines groups producing carbamates.[28] The CO_2–amines interaction and adsorption dynamics in the PEI matrix were thoroughly studied in literature and consists in a rapid interface adsorption followed by a slower diffusion into the bulk of the layer.[29,30] When the sensor chip is heated to >85 °C, CO_2 molecules are released and the amine sorbents in PEI are regenerated.[21] In Figure

https://doi.org/10.1021/acsphotonics.1c01254
ACS Photonics 2022, 9, 34–42

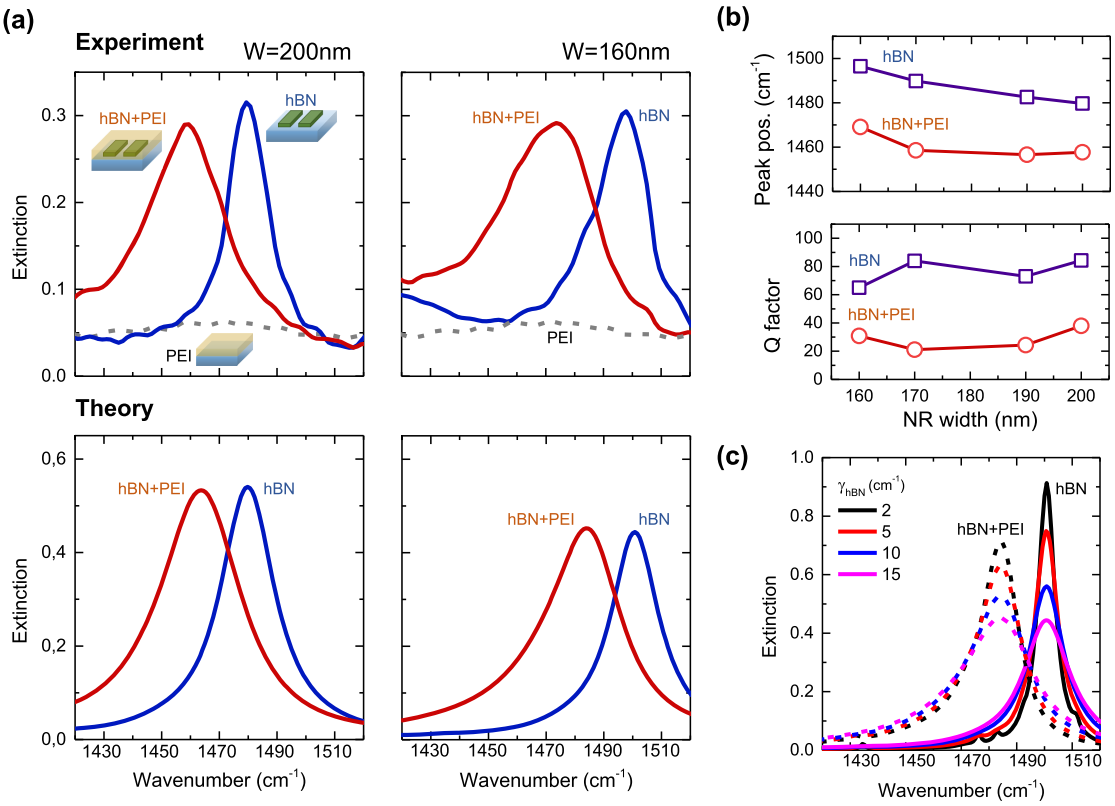

Figure 2. Characterization of hBN nanoribbons modes with functional PEI coating. (a) Experimental (top) and corresponding simulated (bottom) extinction spectra of hBN nanoribbons without (blue) and with (red) PEI layer for two ribbon widths. PEI spectrum is also displayed for comparison (dashed gray). (b) Resonant peak positions and Q factors extracted from experiments for various fabricated ribbon widths without (blue curves) and with (red curves) PEI layer. (c) Simulated PhP resonances of hBN nanoribbons of width 160 nm for different hBN damping values before (solid curves) and after (dashed curves) coating with PEI layer.

1c,d, we report the structural characterizations (scanning electron microscopy SEM and atomic force microscopy AFM) of fabricated hBN nanoribbon array with 400 nm period and 30 nm thickness. Measured IR extinction spectra (see Methods for measurement details) for two hBN nanoribbon arrays in Figure 1b (different ribbon width, same period) show sharp and intense (~30%) PhP resonances. Increasing ribbon width shifts the PhP resonance toward lower wavenumbers, as expected from geometrical tuning above the transverse optical (TO) phonon position.[19] For comparison, the spectrum of a PEI thin film (~75 nm) alone is displayed (gray full line) and rescaled (gray dashed line) to highlight the overlap of the PEI vibrational band at ~1470 cm^{-1} with the PhP resonances.

In the following, we show how the addition of a PEI thin film on top of hBN nanoribbons affects their optical response. We spin coated prepared PEI solution that forms a planar layer (see Methods for preparation and SI.1 for characterizations) entirely covering the hBN nanoribbons (see sensor chip sketch in Figure 1a). The PEI layer is 75 nm thick. Since hBN is approximately 30 nm thick (Figure 1d), we estimate that the PEI layer's thickness on top of hBN is ~45 nm, this value conveniently matching the field decay length of the highly confined hBN PhP modes.[19] Figure 2a shows that addition of PEI on top of hBN nanoribbon arrays (Figure 1b) redshifts and broadens the PhP resonances. Similar effects are experimentally observed for other ribbon widths (see Figure 2b), which reports the extracted values of resonant peak positions and Q factors for several ribbon widths without (blue curve) and with (red curve) PEI coating. The PhP resonances damping can be explained by its coupling to the much broader vibrational resonance of the PEI molecules. Finally, the resonance of the hybrid hBN+PEI system spectrally moves closer to PEI vibration mode at ~1470 cm^{-1}, corresponding to the NCOO skeletal vibration of carbamate,[31] which emerges upon CO_2 adsorption.[22]

Using numerical simulations, we first analyzed the effect of the damping on the PhP modes, that also depends on defects induced by nanofabrication. In Figure 2c, we report the simulated extinction spectra for a representative hBN ribbon array (w = 160 nm) for different hBN damping γ_{hBN} values without (full lines) and with (dashed lines) a planar 75 nm PEI coating. A noticeable drop in the extinction and Q-factor of the PhP mode occurs upon adding PEI layer for low damping values. Our experiments can be reproduced with γ_{hBN} close to 15 cm^{-1}. For such relatively high value of damping, the addition of PEI has negligible effect on the extinction but significantly reduces the Q-factor. In the hBN permittivity model (see Methods) and numerical simulations (lower panel of Figure 2a) for the nanoribbons in combination with a planar 75 nm PEI coating, we used γ_{hBN} = 15 cm^{-1}.

The next part tackles the sensitivity of the proposed sensor to CO_2 gas exposure. To evaluate the sensor response, the surface was exposed to varying concentrations of CO_2 ranging from ambient atmosphere (390 ppm) to higher levels, beyond the classified harmful value (>1000 ppm) in IAQ safety monitoring.[32] The experimental spectra in Figure 3a show that the PhP resonance redshifts, reduces its intensity, and broadens with increasing gas concentration. These changes

https://doi.org/10.1021/acsphotonics.1c01254
ACS Photonics 2022, 9, 34−42

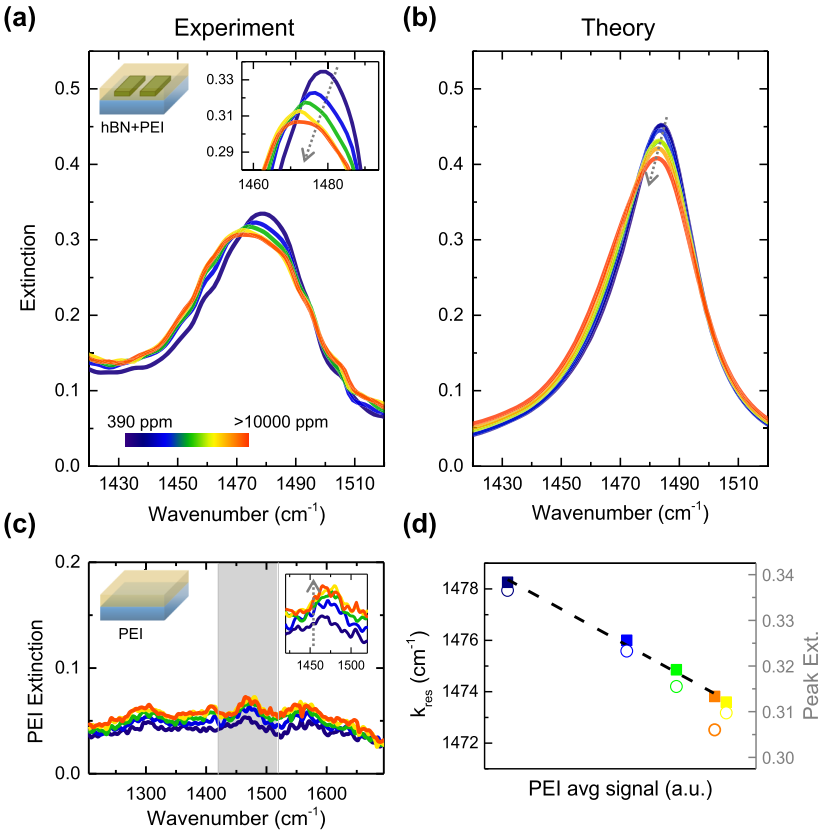

Figure 3. Gas sensor response of hBN+PEI against CO_2 gas concentration. (a) Experimental changes of extinction spectra against increasing CO_2 concentration (direction of gray arrow) expressed in parts per million (ppm). Inset is a zoom-in of peak resonances. (b) Simulated extinction spectra vs increasing CO_2 concentration (see SI for fitted PEI permittivity values). (c) Extinction spectra of bare PEI on CaF_2 against same CO_2 concentration levels as in (a). Inset is a zoom-in of the shaded region. (d) Extracted experimental resonant peak position k_{res} (left axis, solid markers) and peak extinction (right axis, open markers) of PhP modes in (a) as a function of average PEI signal in (c).

are not seen in the control experiment where hBN nanoribbons without PEI layer are exposed to varying CO_2 concentration (see SI.3). Increasing the CO_2 concentration modifies the intensity of the PEI vibrational bands in the range from 1300 to 1700 cm^{-1}, thus, altering its permittivity. Such a change in the dielectric environment induced by the adsorbed CO_2 is then reflected in the modulated PhP resonance. This trend agrees with simulations in Figure 3b (refer to SI.4 for the PEI permittivity fit as a function of CO_2 concentration). The simulated extinction and Q-factor of PhP resonances are higher than those from the experiment. This may be due to nonuniformity and defects of fabricated nanoribbons (e.g., trapezoidal shape, edge sharpness, and ribbon size deviations). Similar trends in the simulated response are obtained for different ribbon widths (see SI.5): (i) PhP resonance redshifts and broadens upon adding PEI, and (ii) PhP resonance further redshifts, reduces in intensity, and broadens with increasing CO_2 concentration. Moreover, SI.2B elucidates the effect of hBN damping and ribbon geometry with the optical response of PhP against the CO_2 concentration. Particularly, lower hBN damping and optimal hBN ribbon width yield high sensitivity against gas exposure, that is, the highest mode extinction difference between atmospheric CO_2 level and high CO_2 concentration. The limit of detection (LOD) of our experiment can be estimated to be equivalent to atmospheric CO_2 concentration (~390 ppm), limited by our gas cell, which is not hermetically sealed.

The hBN+PEI surface allows to transduce gas concentration into PhP resonance modulation with large signal-to-noise ratio (SNR), even under a very small footprint size (30×30 μm^2). In contrast, spectra of PEI only measured with same footprint size (Figure 3c) under same CO_2 level variations yield a poor SNR. The spectra noise floor can be estimated as $N \approx 0.3\%$, which gives $S/N \geq 100$ for the hBN+PEI surface as compared to S/N of ≤ 10 for the bare PEI, that is, more than 10× SNR improvement. This highlights the advantage of utilizing highly confined and low loss hBN PhP modes. Figure 3d shows the extracted peak positions and extinctions of PhP mode in (a) as a function of average PEI signal in (c), representing nominal CO_2 levels. In the explored concentration range we have spectral shift of 4 cm^{-1} and relative extinction reduction of ~10% with respect to the peak values. Note that, for our hBN+PEI surface, monitoring the PhP mode intensity changes upon gas exposure is the most effective way to detect variations in gas concentration. This is because extinction changes are 1 order of magnitude larger than the noise floor (determined as ~0.3%), whereas the overall spectral peak (resonance) shifts are rather small, approaching the spectral resolution (4 cm^{-1}) of the FTIR spectrometer used in the experiments. Additional experiments performed with a thinner (~30 nm) PEI layer show similar but weaker modulation effect upon CO_2 exposure, because less PEI material overlaps with the PhP field (see SI.6). Regarding the gas selectivity, note that the PEI coating prevents direct interaction of hBN with water and other molecules present in the atmosphere. The PhP mode

https://doi.org/10.1021/acsphotonics.1c01254
ACS Photonics 2022, 9, 34−42

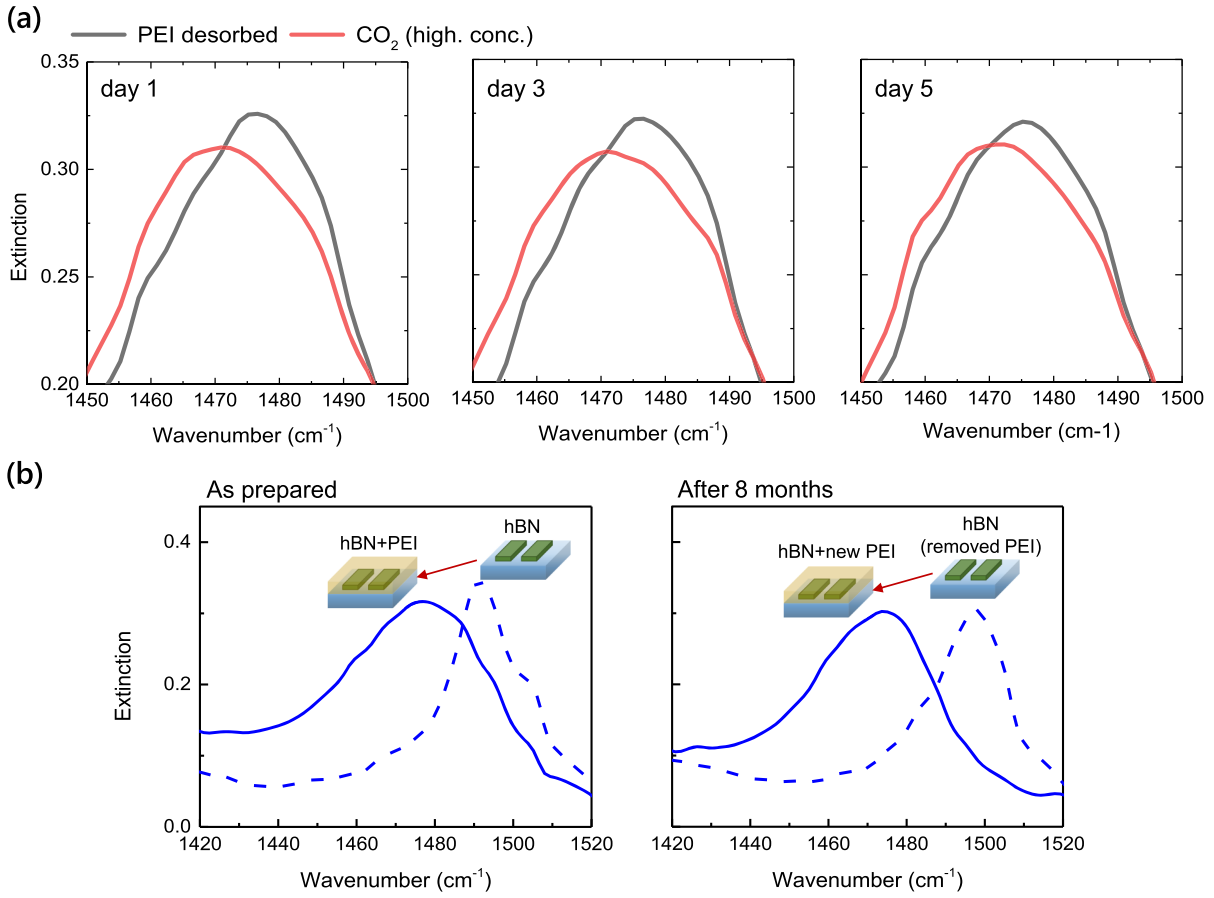

Figure 4. Repeatability and reusability of the CO_2 sensor. (a) Cycles of response measurements upon PEI thermal desorption (gray) and CO_2 gas injection at high concentration (red). (b) Extinction measurements of hBN nanoribbons with and without PEI layer for (left) first time use and (right) removal of old PEI coating and application of new PEI coating after 8 months. The old PEI layer was fully removed with plasma etching.

thus only senses dielectric variations within the PEI layer. Those close to the vibrational mode at ∼1470 cm^{-1} are mostly due to CO_2−amine interactions. PEI interaction with water molecules is negligible around this frequency and mostly observed in the spectral range from 3000 to 3800 cm^{-1}.[33] Beyond CO_2 molecules, PEI can also adsorb and react in a specific way with other gases such as volatile organic compounds (VOCs, e.g., acetone and ethanol) and NH_3.[22,34] However, the PEI vibrational bands that respond to VOCs or NH_3 are also far from the spectral region where PhP modes can be excited.

The sensor response to CO_2 adsorption and desorption has been investigated for several cycles at different days as shown in Figure 4a. For each cycle, the PEI is regenerated by heating the device at 95 °C for 2 min with N_2 gas flow to thermally desorb the CO_2 previously injected. In Figure 1a, we represent the reaction through which the carbamate dissociates to regenerate the amine-sorbents while releasing the CO_2 upon heating.[21,35] Figure 4a shows repeatable response over several days of cycles, consisting of subsequent thermal desorption and re-exposure to high CO_2 levels. Similar behavior occurs upon CO_2 exposure wherein the PhP reduces in intensity and redshifts. We estimate the response time to CO_2 concentration changes of 75 nm PEI to be less than 2 min, in agreement with work of Hasan et al.[22] that reported ∼2 min for 300 nm PEI. Also, in previous work,[24] it was shown that the PEI layer starts to undergo degradation after ∼3 weeks. Thus, stabilizing the PEI coating formulation (e.g., adding cross-linkers during solution preparation) is required to increase the device lifetime.[36,37] For example, the same high molecular weight branched PEI used in this work was combined with mesocelullar foam which resulted in very stable response even after 100 adsorption−desorption cyclic runs.[38] Furthermore, Figure 4b shows the reusability of the sensor. The old PEI layer is removed by oxygen plasma etching after 8 months and the bare hBN nanoribbons regains its PhP resonance at higher wavenumber. Upon addition of new 75 nm PEI coating, the PhP resonance redshifts and broadens, that is consistent with what was described previously. In our proof-of-concept experiment, a simple hBN nanoribbons geometry was used and the coupling of the PhP mode with the gas-sensitive PEI vibrational band was not optimized to fully exploit their high Q. We anticipate that further work employing advanced photonic design (e.g., embedding the hBN+PEI surface in a cavity design[22]) will lead to improved performance with respect to contending systems. The proposed sensing surface can be further improved by reducing fabrication-induced defects, using a larger footprint area (hundreds of μm), and emerging large scale and monolayer hBN (for example by avoiding overlapping of fundamental PhP modes with higher PhP modes[20]). Other gases could be targeted by choosing different gas-adsorbing layer (polymers, metal−organic frameworks, etc.) showing IR-active modes that are affected by the presence of a specific gas within the hBN Reststrahlen band.[39,40] We believe that our work paves the way to the use of high-Q hBN resonant surfaces for applications that go

https://doi.org/10.1021/acsphotonics.1c01254
ACS Photonics 2022, 9, 34−42

beyond the context of a lab experiment with film model molecules such as oxides[41] and CBP[19] layers toward industrial applications, such as environmental sensing.

In summary, we demonstrated a proof-of-concept experiment of phonon polariton-enhanced mid-IR gas sensing using hBN nanoribbons functionalized with CO_2-adsorbing PEI polymer layer. In our system, the PhP resonance is frequency-shifted and weakened with increasing gas concentration due to the change of the local refractive index of the gas absorbing polymer. Moreover, the low loss and high extinction hBN nanoribbon PhP modes allow to sense different CO_2 levels with a large SNR even with a small sensing area (30×30 μm^2). Our results confirm that low-loss phononic materials such as hBN are efficient for surface-enhanced molecular gas sensors. However, further work is needed for a comprehensive comparison with existing SEIRA materials (e.g., metals and graphene), in this way assessing their full potential for applications.

METHODS

Monoisotopic hBN Crystal Growth Method. The ^{10}B-enriched hBN crystals were grown from a metal flux method as described previously.[42] A Ni-Cr-10B powder mixture at respective 48, 48, and 4 wt % was first loaded into an alumina crucible and placed in a single-zone furnace. The furnace was evacuated and then filled with N_2 and H_2 gases to a constant pressure of 850 Torr. During the reaction process, the N_2 and H_2 gases continuously flowed through the system at rates of 125 and 5 sccm, respectively. All the nitrogen in the hBN crystal originated from the flowing N_2 gas. H_2 gas was used to minimize oxygen and carbon impurities in the hBN crystal. After a dwell time of 24 h at 1550 °C, the hBN crystals were precipitated on the metal surface by cooling at a rate of 0.5 °C/h to 1525 °C, and then the system was quickly quenched to room temperature.

EBL Fabrication of hBN Nanoribbons. Mechanically exfoliated monoisotopic hBN flakes were dry transferred onto CaF_2 substrate. High-resolution electron beam lithography was performed with spin-coated PMMA on top of hBN flakes. Different ribbon widths with 400 nm period were patterned on 30×30 μm^2 array elements. PMMA was developed in MIBK/IPA (3:1), then exposed hBN areas were subsequently removed with reactive ion etcher in a SF6/Ar 1:1 plasma mixture at 20 sccm flow, 100 mTorr pressure and 100 W power. Finally, the PMMA mask was removed by immersing the sample overnight in acetone, rinsing it in IPA and drying it using a N_2 gun.

Ultrathin PEI Coating. Branched PEI ($M_w \sim 25000$ from Sigma-Aldrich) was diluted in ethanol by magnetic stirring to obtain 1.58 wt % solution. Prepared PEI solution was spin-coated on top of fabricated hBN nanoribbons at 5000 rpm for 1 min, then baked at 100 °C for 2 min. The PEI characterizations are further detailed in SI.

Infrared Spectrum Measurement. Fourier transmission IR spectrometer (Bruker Tensor II) coupled with an IR microscope (Bruker Hyperion 2000) was used to collect transmission spectra. The incident IR light was polarized perpendicular to long-axis plane of hBN nanoribbons. The beam was focused using a Cassegrain objective (NA = 0.4, 15×) and passed through an aperture window of 30×30 μm^2 that matched the array element size of fabricated regions. The transmitted IR light was collected by liquid nitrogen-cooled mercury−cadmium−tellurium (MCT) detector. Subsequent measurements were taken on the hBN+PEI surface (T, sample) and bare substrate surface (T_0, background) to plot the extinction spectra (Ext = $1 - T/T_0$). The spectral resolution used was 4 cm^{-1}. All the experimental spectra are the average of 100 acquisitions (number of FTIR scans) for a total acquisition time of 1.5 min (signal + background) per displayed spectrum. Subsequent measurements performed on the hBN+PEI and PEI-only surface under the same gas concentration and with the same parameters showed negligible deviations in the observed peak positions and intensities, below the spectral point spacing ($\Delta k = 1.4$ cm^{-1}) and the intensity noise floor ($\Delta I = 0.3\%$). The volume around the optical path and of the gas cell are nitrogen-purged to remove atmospheric gases prior to CO_2 injection. IR fingerprints due to residual atmosphere along the beam path are eliminated when spectra are normalized to calculate extinction.

EM Simulations. Full wave electromagnetic simulations were performed using the COMSOL software based on finite-element methods in frequency domain. In order to achieve convergence, the mesh element size in the vicinity of hBN ribbon was much smaller than the wavelength of excited phonon−polariton.

Dielectric Function Model of PEI and hBN. The dielectric permittivity of CO_2-adsorbed PEI was obtained so that the experimentally measured transmission through 75 nm PEI layer on CaF_2 substrate is reproduced by the analytically computed transmission. For that, the dielectric permittivity of PEI can be expressed as a Lorentz model with three coupled oscillators:

$$\varepsilon_{PEI} = \varepsilon_\infty + \sum_{j=1}^{3} \frac{S_j}{1 - (k/k_{0j})^2 - i\gamma_j(k/k_{0j})}$$

Here, ε^a_∞ represents the high-frequency dielectric constant, S_j is the oscillator strength, k_{0j} is the resonance wavenumber, and γ_j represents the damping factor of the Lorentzian line shapes. The values were obtained through the free parameters when fitting the transmission spectrum. The fitting procedure was made using the MatLab implemented function "nlinfit". This function obtains the fitting parameters using iterative least-squares estimation starting from initial values. The initial values for k_{0j} were those of the resonance wavenumbers in the experimental transmission spectrum and the initial values for S_j and γ_j were ones and zeros, respectively. The fitted parameters for different CO_2 concentrations are summarized in Table S1 in the SI.

The dielectric function of hBN was extracted by fitting various transmission spectra through nonpatterned hBN flakes with several thicknesses on CaF_2 substrates. The collection of spectra were fitted using analogous approach as the one described above for extracting the dielectric function of PEI. The in-plane $\varepsilon_\perp$ and out-of-plane $\varepsilon_\parallel$ dielectric permittivity of hBN, can be expressed in the single-Lorentzian form:

$$\varepsilon_a = \varepsilon^a_\infty \left(1 + \frac{[\omega^a_{LO}]^2 - [\omega^a_{TO}]^2}{[\omega^a_{TO}]^2 - \omega^2 - i\omega\gamma_a}\right)$$

where a refers to either the transverse ($\perp$ or a,b crystal plane) or z ($\parallel$ or c crystal axis) axes, ε^a_∞ represents the high-frequency dielectric constant, ω^a_{TO} and ω^a_{LO} refer to the transverse (TO) and longitudinal (LO) phonon−polariton frequencies, respectively; and γ_a represents the damping factor. The free parameters ε^a_∞, ω^a_{TO}, ω^a_{LO}, and γ_a were fitted to reproduce

https://doi.org/10.1021/acsphotonics.1c01254
ACS Photonics 2022, 9, 34−42

the experimentally obtained transmission spectrum through hBN on CaF_2 substrate. As before, the fitting procedure was made using Matlab implemented function "nlinfit". The initial guess for the parameters ε_{∞}^{a}, ω_{TO}^{a}, ω_{LO}^{a}, and γ_a was taken from ref 13. With the procedure we obtain $\varepsilon_{\infty}^{\perp} = 6.1$, $\omega_{TO}^{\perp} = 1395$ cm^{-1}, $\omega_{LO}^{\perp} = 1630$ cm^{-1}, $\gamma_{\perp} = 8$ cm^{-1}, $\varepsilon_{\infty}^{\parallel} = 2.8$, $\omega_{TO}^{\parallel} = 785$ cm^{-1}, $\omega_{LO}^{\parallel} = 845$ cm^{-1}, and $\gamma_{\parallel} = 1$ cm^{-1}. The calculations of the transmission spectra through patterned hBN on CaF_2 systems produce resonant values that are larger than the experimental ones, which we associate to imperfections created in the actual sample during fabrication. We have found that this effect can be taken into account by adjusting $\gamma_{\perp}$ close to 15 cm^{-1}.

■ ASSOCIATED CONTENT

Supporting Information

The Supporting Information is available free of charge at https://pubs.acs.org/doi/10.1021/acsphotonics.1c01254.

(S1) Thin PEI film characterizations such as thickness, surface morphology and deposited layer profile. (S2) Differential resonant extinction contour plots as functions of hBN damping and ribbon geometry. (S3) Sensing of bare hBN nanoribbons with varying CO_2 concentration. (S4) Fit of PEI permittivity model from experimental transmission spectrum as a function of CO_2 concentration. (S5) Simulated response of different hBN ribbon geometry in varying CO_2 concentration. (S6) Sensing of hBN nanoribbons and 30 nm PEI coating with varying CO_2 concentration (PDF)

■ AUTHOR INFORMATION

Corresponding Author

Bruno Paulillo − *ICFO-Institut de Ciencies Fotoniques, The Barcelona Institute of Science and Technology, Castelldefels, Barcelona 08860, Spain;* orcid.org/0000-0002-6675-0141; Email: bruno.paulillo@icfo.eu

Authors

Nestor Jr. Bareza − *ICFO-Institut de Ciencies Fotoniques, The Barcelona Institute of Science and Technology, Castelldefels, Barcelona 08860, Spain*

Tetiana M. Slipchenko − *INMA-Instituto de Nanociencia y Materiales de Aragón, CSIC-Universidad de Zaragoza, Zaragoza 50009, Spain; Departamento de Física de la Materia Condensada, Universidad de Zaragoza, Zaragoza 50009, Spain;* orcid.org/0000-0003-3918-0275

Marta Autore − *CIC nanoGUNE BRTA, Donostia-San Sebastián 20018, Spain*

Irene Dolado − *CIC nanoGUNE BRTA, Donostia-San Sebastián 20018, Spain*

Song Liu − *Tim Taylor Department of Chemical Engineering, Kansas State University, Manhattan, Kansas 66506, United States*

James H. Edgar − *Tim Taylor Department of Chemical Engineering, Kansas State University, Manhattan, Kansas 66506, United States;* orcid.org/0000-0003-0918-5964

Saül Vélez − *CIC nanoGUNE BRTA, Donostia-San Sebastián 20018, Spain; IFIMAC-Condensed Matter Physics Center and Departamento de Física de la Materia Condensada, Universidad Autónoma de Madrid, Madrid E-28049, Spain*

Luis Martín-Moreno − *INMA-Instituto de Nanociencia y Materiales de Aragón, CSIC-Universidad de Zaragoza, Zaragoza 50009, Spain; Departamento de Física de la Materia Condensada, Universidad de Zaragoza, Zaragoza 50009, Spain;* orcid.org/0000-0001-9273-8165

Rainer Hillenbrand − *CIC nanoGUNE BRTA and Department of Electricity and Electronics, UPV/EHU, Donostia-San Sebastián 20018, Spain; IKERBASQUE, Basque Foundation for Science, Bilbao 48009, Spain;* orcid.org/0000-0002-1904-4551

Valerio Pruneri − *ICFO-Institut de Ciencies Fotoniques, The Barcelona Institute of Science and Technology, Castelldefels, Barcelona 08860, Spain; ICREA-Institució Catalana de Recerca i Estudis Avançats, Barcelona 08010, Spain*

Complete contact information is available at: https://pubs.acs.org/10.1021/acsphotonics.1c01254

Funding

The research leading to these results has received funding from the H2020 Programme under Grant Agreement No. 881603 (Graphene Flagship). This project has received funding from the European Union's Horizon 2020 research and innovation program under the Marie Sklodowska-Curie Grant Agreement No. 754510. This project has received funding from the European Union's Horizon 2020 research and innovation program under the Marie Sklodowska-Curie Grant Agreement No. 665884. This work was partially funded by CEX2019-000910-S [MICINN/AEI/10.13039/501100011033] and Project TUNA-SURF (PID2019-106892RB-I00), Fundació Cellex, Fundació Mir-Puig, and Generalitat de Catalunya through CERCA. We acknowledge financial support from the Spanish Ministry of Science, Innovation and Universities (RTI2018-094830-B-100 and the Project MDM-2016-0618 of the Maria de Maeztu Units of Excellence Program) and the Basque Government (Grant Number IT1164-19). We acknowledge the Ministry of Science, Innovation and Universities through the 'Maria de Maezt' Programme for Units of Excellence in R&D (CEX2018-000805-M). Further, support from the Materials Engineering and Processing program of the National Science Foundation, Award Number CMMI 1538127 for h-BN crystal growth is greatly appreciated. The hBN crystals growth is also supported by an Office of Naval Research Award No. N00014-20-1-2474. I.D. acknowledges the Basque Government (Grant No. PRE_2019_2_0164). We acknowledge Project PID2020-115221GB-C41 financed by MCIN/AEI/10.13039/501100011033 and Aragon Government through Project Q-MAD.

Notes

The authors declare no competing financial interest.

■ ACKNOWLEDGMENTS

We thank Daniel Martinez for help with AFM measurements.

■ REFERENCES

(1) Wong, J. Y. NDIR Gas Sensor. US5747808A, 1998.

(2) Stolberg-Rohr, T.; Buchner, R.; Clausen, S.; Jensen, J. M.; Skouboe, A.; Hawkins, G.; Hansen, R. S. In Optics Humidity Compensation in NDIR Exhaust Gas Measurements of NO_2. *Optical Sensors, 2014*; Optical Society of America, 2014; paper SeTh1C.3, DOI: 10.1364/SENSORS.2014.SeTh1C.3.

(3) Wang, H.; Chen, J.; Lu, K. Development of a Portable Cavity-Enhanced Absorption Spectrometer for the Measurement of Ambient NO_3 and N_2O_5: Experimental Setup, Lab Characterizations, and Field

Applications in a Polluted Urban Environment. *Atmos. Meas. Tech.* **2017**, *10*, 1465.
(4) Brown, S. S.; Stark, H.; Ravishankara, A. R. Cavity Ring-down Spectroscopy for Atmospheric Trace Gas Detection: Application to the Nitrate Radical (NO3). *Appl. Phys. B: Lasers Opt.* **2002**, *75*, 173.
(5) Patimisco, P.; Scamarcio, G.; Tittel, F. K.; Spagnolo, V. Quartz-Enhanced Photoacoustic Spectroscopy: A Review. *Sensors* **2014**, *14* (4), 6165−6206.
(6) Neubrech, F.; Huck, C.; Weber, K.; Pucci, A.; Giessen, H. Surface-Enhanced Infrared Spectroscopy Using Resonant Nano-antennas. *Chem. Rev.* **2017**, *117*, 5110.
(7) Cubukcu, E.; Zhang, S.; Park, Y. S.; Bartal, G.; Zhang, X. Split Ring Resonator Sensors for Infrared Detection of Single Molecular Monolayers. *Appl. Phys. Lett.* **2009**, *95* (4), 043113.
(8) Gopalan, K. K.; Paulillo, B.; Mackenzie, D. M. A.; Rodrigo, D.; Bareza, N.; Whelan, P. R.; Shivayogimath, A.; Pruneri, V. Scalable and Tunable Periodic Graphene Nanohole Arrays for Mid-Infrared Plasmonics. *Nano Lett.* **2018**, *18* (9), 5913−5918.
(9) Lilley, G.; Messner, M.; Unterrainer, K. Improving the Quality Factor of the Localized Surface Plasmon Resonance. *Opt. Mater. Express* **2015**, *5* (10), 2112.
(10) Rodrigo, D.; Limaj, O.; Janner, D.; Etezadi, D.; García De Abajo, F. J.; Pruneri, V.; Altug, H. Mid-Infrared Plasmonic Biosensing with Graphene. *Science* **2015**, *349* (6244), 165−168.
(11) Paulillo, B.; Bareza, N. J.; Pruneri, V. Controlling Mid-Infrared Plasmons in Graphene Nanostructures through Post-Fabrication Chemical Doping. *J. Phys.: Photonics* **2021**, *3* (3), 034001.
(12) Apalkov, V.; Stockman, M. I. Proposed Graphene Nanospaser. *Light: Sci. Appl.* **2014**, *3*, e191.
(13) Caldwell, J. D.; Kretinin, A. v.; Chen, Y.; Giannini, V.; Fogler, M. M.; Francescato, Y.; Ellis, C. T.; Tischler, J. G.; Woods, C. R.; Giles, A. J.; Hong, M.; Watanabe, K.; Taniguchi, T.; Maier, S. A.; Novoselov, K. S. Sub-Diffractional Volume-Confined Polaritons in the Natural Hyperbolic Material Hexagonal Boron Nitride. *Nat. Commun.* **2014**, *5*, 5221 DOI: 10.1038/ncomms6221.
(14) Basov, D. N.; Fogler, M. M.; García De Abajo, F. J. Polaritons in van Der Waals Materials. *Science* **2016**, DOI: 10.1126/science.aag1992.
(15) Giles, A. J.; Dai, S.; Vurgaftman, I.; Hoffman, T.; Liu, S.; Lindsay, L.; Ellis, C. T.; Assefa, N.; Chatzakis, I.; Reinecke, T. L.; Tischler, J. G.; Fogler, M. M.; Edgar, J. H.; Basov, D. N.; Caldwell, J. D. Ultralow-Loss Polaritons in Isotopically Pure Boron Nitride. *Nat. Mater.* **2018**, *17* (2), 134.
(16) Ma, W.; Alonso-González, P.; Li, S.; Nikitin, A. Y.; Yuan, J.; Martín-Sánchez, J.; Taboada-Gutiérrez, J.; Amenabar, I.; Li, P.; Vélez, S.; Tollan, C.; Dai, Z.; Zhang, Y.; Sriram, S.; Kalantar-Zadeh, K.; Lee, S. T.; Hillenbrand, R.; Bao, Q. In-Plane Anisotropic and Ultra-Low-Loss Polaritons in a Natural van Der Waals Crystal. *Nature* **2018**, *562* (7728), 557.
(17) Taboada-Gutiérrez, J.; Álvarez-Pérez, G.; Duan, J.; Ma, W.; Crowley, K.; Prieto, I.; Bylinkin, A.; Autore, M.; Volkova, H.; Kimura, K.; Kimura, T.; Berger, M. H.; Li, S.; Bao, Q.; Gao, X. P. A.; Errea, I.; Nikitin, A. Y.; Hillenbrand, R.; Martín-Sánchez, J.; Alonso-González, P. Broad Spectral Tuning of Ultra-Low-Loss Polaritons in a van Der Waals Crystal by Intercalation. *Nat. Mater.* **2020**, *19* (9), 964.
(18) Li, P.; Dolado, I.; Alfaro-Mozaz, F. J.; Nikitin, A. Y.; Casanova, F.; Hueso, L. E.; Vélez, S.; Hillenbrand, R. Optical Nanoimaging of Hyperbolic Surface Polaritons at the Edges of van Der Waals Materials. *Nano Lett.* **2017**, *17* (1), 228.
(19) Autore, M.; Li, P.; Dolado, I.; Alfaro-Mozaz, F. J.; Esteban, R.; Atxabal, A.; Casanova, F.; Hueso, L. E.; Alonso-González, P.; Aizpurua, J.; Nikitin, A. Y.; Vélez, S.; Hillenbrand, R. Boron Nitride Nanoresonators for Phonon-Enhanced Molecular Vibrational Spectroscopy at the Strong Coupling Limit. *Light: Sci. Appl.* **2018**, *7*, 17172.
(20) Autore, M.; Dolado, I.; Li, P.; Esteban, R.; Alfaro-Mozaz, F. J.; Atxabal, A.; Liu, S.; Edgar, J. H.; Vélez, S.; Casanova, F.; Hueso, L. E.; Aizpurua, J.; Hillenbrand, R. Enhanced Light−Matter Interaction in 10B Monoisotopic Boron Nitride Infrared Nanoresonators. *Adv. Opt. Mater.* **2021**, *9* (5), 2001958.
(21) Drage, T. C.; Smith, K. M.; Arenillas, A.; Snape, C. E. Developing Strategies for the Regeneration of Polyethylenimine Based CO_2 Adsorbents. *Energy Procedia* **2009**, *1*, 875−880.
(22) Hasan, D.; Lee, C. Hybrid Metamaterial Absorber Platform for Sensing of CO_2 Gas at Mid-IR. *Advanced Science* **2018**, *5* (5), 1700581.
(23) Pohl, T.; Sterl, F.; Strohfeldt, N.; Giessen, H. Optical Carbon Dioxide Detection in the Visible down to the Single Digit Ppm Range Using Plasmonic Perfect Absorbers. *ACS Sensors* **2020**, *5* (8), 2628.
(24) Bareza, N. J.; Gopalan, K. K.; Alani, R.; Paulillo, B.; Pruneri, V. Mid-Infrared Gas Sensing Using Graphene Plasmons Tuned by Reversible Chemical Doping. *ACS Photonics* **2020**, *7* (4), 879.
(25) Chang, Y.; Hasan, D.; Dong, B.; Wei, J.; Ma, Y.; Zhou, G.; Ang, K. W.; Lee, C. All-Dielectric Surface-Enhanced Infrared Absorption-Based Gas Sensor Using Guided Resonance. *ACS Appl. Mater. Interfaces* **2018**, *10* (44), 38272−38279.
(26) Kwon, J.; Ahn, G.; Kim, G.; Kim, J. C.; Kim, H. A Study on NDIR-Based CO_2 Sensor to Apply Remote Air Quality Monitoring System. *ICCAS-SICE 2009 - ICROS-SICE International Joint Conference 2009 Proceedings*, Fukuoka, Japan, Aug 18−21, 2009, IEEE, 2009.
(27) Pitarma, R.; Marques, G.; Ferreira, B. R. Monitoring Indoor Air Quality for Enhanced Occupational Health. *Journal of Medical Systems* **2017**, DOI: 10.1007/s10916-016-0667-2.
(28) Wang, X.; Schwartz, V.; Clark, J. C.; Ma, X.; Overbury, S. H.; Xu, X.; Song, C. Infrared Study of CO 2 Sorption over "Molecular Basket" Sorbent Consisting of Polyethylenimine-Modified Mesoporous Molecular Sieve. *J. Phys. Chem. C* **2009**, *113*, 7260.
(29) Sharma, P.; Chakrabarty, S.; Roy, S.; Kumar, R. Molecular View of CO2 Capture by Polyethylenimine: Role of Structural and Dynamical Heterogeneity. *Langmuir* **2018**, *34* (17), 5138.
(30) Al-Marri, M. J.; Khader, M. M.; Tawfik, M.; Qi, G.; Giannelis, E. P. CO_2 Sorption Kinetics of Scaled-up Polyethylenimine-Functionalized Mesoporous Silica Sorbent. *Langmuir* **2015**, *31* (12), 3569.
(31) Hiyoshi, N.; Yogo, K.; Yashima, T. Adsorption Characteristics of Carbon Dioxide on Organically Functionalized SBA-15. *Microporous Mesoporous Mater.* **2005**, *84*, 357.
(32) Mumma, S. a. Transient Occupancy Ventilation By Monitoring CO_2. *IAQ Applications* **2004**, *5* (1), 21−23.
(33) Liu, J. Multilayered PEI-Based Films for CO_2 Adsorption and Diffusion. *Master's thesis*, University of Akron, 2013. http://rave.ohiolink.edu/etdc/view?acc_num=akron1367839488.
(34) Lin, Y.; Kan, K.; Song, W.; Zhang, G.; Dang, L.; Xie, Y.; Shen, P.; Li, L.; Shi, K. Controllable Synthesis of Co3O4/Polyethyleneimine-Carbon Nanotubes Nanocomposites for CO and NH_3 Gas Sensing at Room Temperature. *J. Alloys Compd.* **2015**, *639*, 187.
(35) Chowdhury, F. A.; Yamada, H.; Higashii, T.; Goto, K.; Onoda, M. CO2 Capture by Tertiary Amine Absorbents: A Performance Comparison Study. *Ind. Eng. Chem. Res.* **2013**, *52*, 8323.
(36) Zhang, S.; Kang, P.; Ubnoske, S.; Brennaman, M. K.; Song, N.; House, R. L.; Glass, J. T.; Meyer, T. J. Polyethylenimine-Enhanced Electrocatalytic Reduction of CO2 to Formate at Nitrogen-Doped Carbon Nanomaterials. *J. Am. Chem. Soc.* **2014**, *136*, 7845.
(37) Zhai, Y.; Chuang, S. S. C. Enhancing Degradation Resistance of Polyethylenimine for CO2 Capture with Cross-Linked Poly(Vinyl Alcohol). *Ind. Eng. Chem. Res.* **2017**, *56* (46), 13766.
(38) Zhang, H.; Goeppert, A.; Czaun, M.; Prakash, G. K. S.; Olah, G. A. CO_2 Capture on Easily Regenerable Hybrid Adsorbents Based on Polyamines and Mesocellular Silica Foam. Effect of Pore Volume of the Support and Polyamine Molecular Weight. *RSC Adv.* **2014**, *4* (37), 19403.
(39) Zoshki, A.; Rahmani, M. B.; Masdarolomoor, F.; Pilehrood, S. H. Room Temperature Gas Sensing Properties of Polyaniline/ZnO Nanocomposite Thin Films. *J. Nanoelectron. Optoelectron.* **2017**, *12* (5), 465.
(40) Zhou, H.; Hui, X.; Li, D.; Hu, D.; Chen, X.; He, X.; Gao, L.; Huang, H.; Lee, C.; Mu, X. Metal−Organic Framework-Surface-Enhanced Infrared Absorption Platform Enables Simultaneous On-

Chip Sensing of Greenhouse Gases. *Advanced Science* **2020**, *7* (20), 2001173.
(41) Berte, R.; Gubbin, C. R.; Wheeler, V. D.; Giles, A. J.; Giannini, V.; Maier, S. A.; de Liberato, S.; Caldwell, J. D. Sub-Nanometer Thin Oxide Film Sensing with Localized Surface Phonon Polaritons. *ACS Photonics* **2018**, *5* (7), 2807.
(42) Liu, S.; He, R.; Xue, L.; Li, J.; Liu, B.; Edgar, J. H. Single Crystal Growth of Millimeter-Sized Monoisotopic Hexagonal Boron Nitride. *Chem. Mater.* **2018**, *30* (18), 6222.

https://doi.org/10.1021/acsphotonics.1c01254
ACS Photonics 2022, 9, 34−42